doi:10.26443/seismica.v5i1.1720

Designing small-aperture seismic arrays to enhance earthquake monitoring on ocean islands: Application to Antikythera island, Greece

Konstantinos Lentas * [1], **Christos P. Evangelidis** [1], **Vassilios Karastathis** [1]

[1]Institute of Geodynamics, National Observatory of Athens, Lofos Nymfon, Athens, 11810, Greece

Author contributions: *Conceptualization*: Christos Evangelidis, Konstantinos Lentas. *Methodology*: Konstantinos Lentas. *Software*: Konstantinos Lentas. *Resources*: Christos Evangelidis, Vassilios Karastathis. *Writing - Original draft*: Konstantinos Lentas. *Writing - Review & Editing*: Konstantinos Lentas, Christos Evangelidis, Vassilios Karastathis. *Project administration*: Christos Evangelidis.

Abstract We present an optimisation strategy in order to design a seismic array at the Antikythera island (Greece), consisted of nine elements in total, namely, eight new and one permanent station. This new seismic array aims to improve the seismic event detection capability and location accuracy of the Hellenic Unified Seismic Network (HUSN) at the SW-end of Greece, for local and regional seismicity, which is constrained by the sparse station coverage between Peloponnese and Crete. Instead of simply being based on theoretical transfer function calculations, we set up a synthetic dataset of realistic seismic sources and we determine the backazimuth and slowness vectors based on array beamforming via a global optimisation scheme that takes into account several criteria, such as amplitude power, event mislocation, array shape and landscape restrictions. The result is a set of station coordinates whose positions shape different array configurations at each step of the optimisation process, affecting both the maximum amplitude beam of P and S wavefields, as well as the ability of each array configuration to successfully resolve the backazimuth of each seismic source. The optimal array is determined as the one associated with the minimum score of an objective function based on the above criteria, being an irregular shaped array with an aperture of ∼4.0 km.

Production Editor:
Andrea Llenos
Handling Editor:
Stephen Hicks
Copy & Layout Editor:
Anna M. Ledeczi

Signed reviewer(s):
Roberto Cabieces Díaz

Received:
May 7 2025
Accepted:
January 28 2026
Published:
February 11 2026

1 Introduction

Earthquake monitoring in oceanic environments can usually be challenging depending on the spatial distribution of islands and their accessibility or lack of infrastructure. Depending on the application, parts of the vast oceans can be covered by Ocean Bottom Seismometers (OBS), nevertheless, their deployment and maintenance can be very expensive. Moreover, OBS deployments usually suffer from timing and positioning errors, and the instruments orientation can only be determined by applying numerical techniques (Stachnik et al., 2012; Scholz et al., 2016; Trabattoni et al., 2019; Zhu et al., 2020). On the other hand, seismic arrays can offer an alternative option to achieve better detection capabilities and earthquake location accuracy especially in regional and teleseismic distance ranges (Kværna and Ringdal, 2013).

A seismic array is a set of seismometers arranged in either a regular geometric pattern (circle, rectangle, cross) or an irregular configuration over a relatively homogeneous geological setting that ensures high signal coherence between the recordings of individual array elements. This arrangement can lead to random noise suppression, and hence, the enhancement of the signal-to-noise ratio (SNR), after applying array techniques (i.e., Capon et al., 1967; Kværna and Ringdal, 1986; Rost and Thomas, 2002) in order to increase the sensitivity to seismic event detection and estimate the slowness vector.

Seismic arrays were first implemented in the 1950s in order to improve the detection of nuclear tests worldwide, whereas, today, many seismic arrays are used by the International Monitoring System (IMS) for the Comprehensive Nuclear-Test-Ban Treaty Organization (CTBTO, Bungum et al., 1971; Ringdal and Husebye, 1982; Schweitzer, 2001; Kværna et al., 2002; Haak et al., 2009; Gibbons, 2012; Gibbons et al., 2015, 2017; Kværna et al., 2021). Small-aperture arrays have also been employed to study microseisms and aftershock sequences (i.e., Capon, 1969; Mykkeltveit and Bungum, 1984; Cessaro and Chan, 1989; Frankel et al., 1991; Friedrich et al., 1998; Stump, 2004; La Rocca et al., 2008), as well as a tool for monitoring and locating volcanic tremors (i.e., Furumoto et al., 1990; Goldstein and Chouet, 1994; Métaxian et al., 1997; Almendros et al., 2014; Hata et al., 2024). Large-aperture seismic arrays based on ocean bottom seismometers (OBS) have been also implemented (i.e., Cabieces et al., 2020; Wei et al., 2020; Eilon et al., 2021; Lontsi et al., 2021; Cabieces et al., 2024), and recently, Distributed Acoustic Sensing (DAS) systems have been tested in array configuration, in order to enhance seismic monitoring and earthquake location (i.e., Lindsey et al., 2017; Ajo-Franklin et al., 2019; Lindsey et al., 2020; Hudson et al., 2021; Klaasen et al., 2021; van den Ende

*Corresponding author: k.lentas@noa.gr

and Ampuero, 2021; Näsholm et al., 2022; Lentas et al., 2023; Miao et al., 2024). Seismic arrays can vary in geometry, aperture and number of seismometers in order to achieve high resolution of the calculated slowness vector.

The simplest way to design a seismic array is based on the estimation of the transfer function, which describes the resolution of an array for a specific geometry, for seismic signals at different frequencies and slownesses. Selecting the proper number of stations and aperture is key for the analysis of a finite wavelength range of a seismic signal, since the aperture and inter-station distances of the array control its resolution (Schweitzer et al., 2009). Nevertheless, using only the theoretical array transfer function as a design tool for an array with predefined shape, may ignore other parameters, such as, the impact of using different geometries to control sensitivity azimuthal effects and/or earthquake mechanism effects, namely, the impact of the radiation patterns of different body-wave types.

In order to address this, another technique in array design is to maximise the gain of the seismic signal through beamforming. For any array geometry the signal-to-noise ratio gain is defined as the ratio of the signal cross-correlation over the noise cross-correlation between array sensors. This process is based on real data recorded during experimental site surveys, meaning that sensors can move around the deployment site over different time intervals. Although this technique is time consuming, and most likely high cost, it provides at least a quantitative measure of the array performance under real conditions. This was the approach followed for the design of the NORES array in Norway in 1984 (Mykkeltveit, 1985).

On the other hand, Karamzadeh et al. (2018) followed a different approach in order to take into account the resolution and gain effects in seismic array design simultaneously, by setting up a synthetic test. Specifically, they used a grid search technique to determine the optimal layout of a small-scale array that would monitor an earthquake swarm in the NW Bohemia. Their work offers the advantage of a quick, and cost effective way to customise the array design according to the needs of a specific site and taking into account the source characteristics of target seismic events, without pre-installing test arrays on the field. As a result, they were able to achieve higher resolution slowness estimation against the use of regular seismic array designs.

The goal of this study is to present a generic framework to design seismic arrays based on location accuracy criteria as well as taking into account spatial constraints usually applying in small and remote islands with limited infrastructure. Nevertheless, the framework proposed in the current study can be adapted to any other place onshore or offshore. For this purpose we design a new seismic array consisted of nine stations, namely, eight new three-component broadband seismic stations, which will be deployed at the Antikythera island, in conjunction with the permanent seismic station ANKY (Antikythera, National Observatory of Athens, Institute of Geodynamics, Athens, 1975). Antikythera is a small island that lies at the west-end of the Aegean Sea, between Crete and Peloponnese (Fig. 1), measuring approximately 10.5 km NNW to SSE by 3.4 km ENE to WSW, covering a land area of approximately 20 km^2. Its position is ideal for monitoring the seismic activity of the Hellenic Subduction Zone, which constitutes the convergent boundary between the African plate and the Eurasian plate at a rate of approximately 3.5 cm/yr - 4.0 cm/yr (i.e., Pichon and Angelier, 1979; DeMets et al., 1990; McClusky et al., 2000).

In the remainder of this paper we will be describing the framework that we followed in order to design the optimal seismic array for the Antikythera island, based in essence on a grid search technique similar to Karamzadeh et al. (2018), but following different constraints that suited better our case. First we explain how we created the dataset, and then we set up our optimisation strategy based on a synthetic, but realistic, earthquake location problem. Finally, we present our results and discuss the findings of our work and its implications.

2 Data

We used 48 Centroid Moment Tensor solutions (GCMT, Dziewonski et al., 1981; Ekström et al., 2012) from 1977 to 2014, with M_W ranging from 4.7 to 6.2, distributed along the SW portion of the Hellenic Subduction Zone. This dataset was complemented with 23 moment tensors from the National Observatory of Athens database (NOA, Triantafyllis et al., 2021) from 2014 to 2024, with $M_W < 4.7$ (Fig. 1). The majority of this seismicity is characterised by thrust mechanism earthquakes along the subduction zone, right-lateral strike-slip mechanisms at the NW part of the study area, and some oblique mechanism earthquakes to the SW of Crete, whilst the earthquake depth range is between 20 km and 50 km. A few shallow, normal fault earthquake mechanisms are observed at south Crete.

The dataset was classified by mechanism type in five distinct clusters (Álvarez Gómez, 2019), as shown in the Kaverina diagram (Kaverina et al., 1996) of Fig. S1a in the Supplementary material, without following a clear geographical distribution with mechanism type, highlighting the complex tectonics of the SW Hellenic Subduction Zone (Fig. S1b in the Supplementary material). We then split the area in $1^\circ \times 1^\circ$ grid cells, and within each cell, and for each mechanism type cluster, the median hypocentre and moment tensor was calculated, defining 23 distinct seismic sources (Fig. S2 in the Supplementary material). The results of this process are summarised in Tab. 1.

3 Methods

In order to design the nine-element (including one permanent station) seismic array on Antikythera island on a consistent and data driven way, we set up a grid search technique, with the objective to determine the optimal position of each one of the eight newly deployed stations, expressed by their geographic latitude and longitude pairs (φ_j, λ_j, with $j \in [1, 8]$). It is worth clarifying that the location of the permanent station ANKY

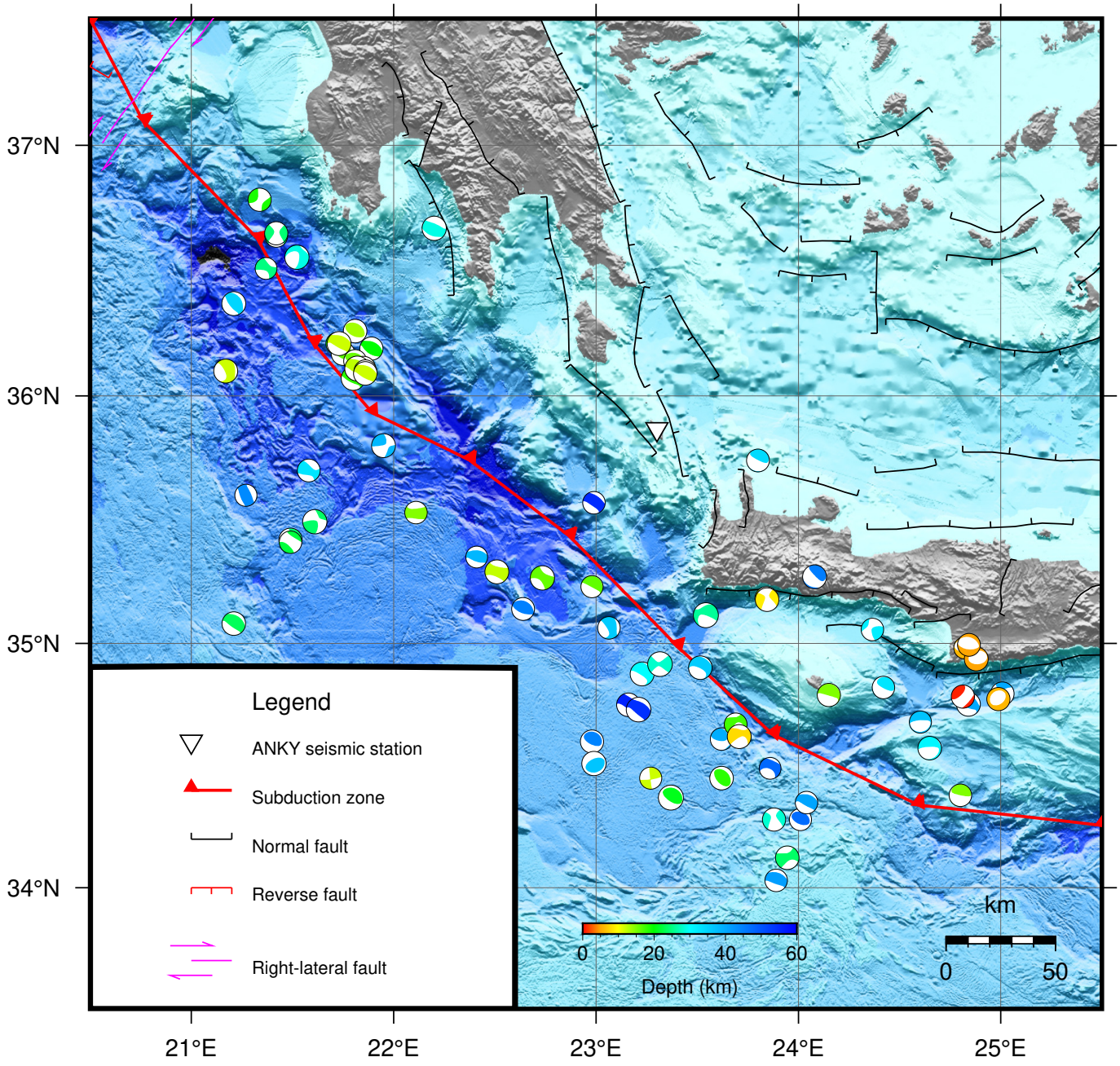

Figure 1 Map showing the location of the ANKY station (Antikythera, National Observatory of Athens, Institute of Geodynamics, Athens, 1975, inverse triangle) and the spatial distribution of the earthquake moment tensors used in the current study, colour-coded by depth. The Hellenic Subduction Zone and main seismic faults obtained from the GEM active fault database (Styron and Pagani, 2020) are plotted according to the map legend.

which will be part of the array, is not allowed to change, thus, even though the array is consisted of nine stations in total, the grid search is carried out on a 16-parameter model space ($\mathbb{S}$), where each model (m, $m \subset \mathbb{S}$) is expressed in a vector form as (T denotes the transpose form):

$$m = [\varphi_1 \quad \lambda_1 \quad \varphi_2 \quad \lambda_2 \quad \dots \quad \varphi_8 \quad \lambda_8]^T \qquad (1)$$

Nevertheless, the permanent station ANKY is added separately on a later step, and being taken into account in the calculations during the grid search as the ninth element of the array.

In the following sub-sections we will discuss all the necessary components in order to set up our technique, namely, spatial constraints associated with the topography and geometrical features of the seismic array, synthetic waveforms and processing, as well as the optimisation strategy.

3.1 Spatial constraints

Each model (m), namely, the positions of the seismic array elements are subject to several geometric and geographic constraints, given the size and topography of the Antikythera island. The range of each parameter in the parameter space is defined by two values (minimum and maximum), and all station latitudes and longitudes have the same range respectively ($\varphi_j \in$ [35.835, 35.885],

Index	Latitude (°)	Longitude (°)	Depth (km)	Strike (°)	Dip (°)	Rake (°)	Δ (km)	Backazimuth (°)
1	34.56	22.99	40.6	241	55	74	148.7	191.3
2	34.62	23.71	8.0	48	88	38	143.5	164.9
3	34.45	23.37	41.4	132	56	92	157.7	177.7
4	34.61	23.62	39.5	101	76	58	142.7	168.2
5	34.94	24.84	5.0	69	57	-82	173.9	306.8
6	34.35	24.04	40.6	117	62	90	181.6	158.0
7	34.81	24.29	24.0	110	86	93	148.0	323.1
8	35.70	21.58	33.0	78	61	30	156.4	263.7
9	35.49	21.61	24.0	265	78	156	158.2	255.3
10	35.34	21.24	33.6	131	58	85	195.3	253.2
11	35.29	22.51	12.4	247	65	23	96.1	228.5
12	35.27	22.74	16.0	262	79	3	84.2	217.8
13	35.35	22.64	45.0	114	58	87	82.9	226.4
14	35.23	22.98	16.2	118	86	87	76.6	202.5
15	35.15	23.69	19.0	303	85	-139	87.4	155.9
16	35.06	23.06	36.0	137	78	55	92.0	193.7
17	35.06	24.37	32.0	259	70	15	132.0	132.6
18	35.27	24.08	45.3	318	81	-78	96.8	132.9
19	36.64	21.42	24.8	223	72	-18	189.3	297.5
20	36.56	21.52	29.0	261	43	-26	177.0	296.0
21	36.14	21.81	13.6	117	56	89	137.5	283.1
22	36.10	21.17	12.0	144	82	64	193.5	278.3
23	36.67	22.20	29.0	295	56	93	133.1	312.3

Table 1 Table summarising the details of the 23 distinct seismic sources determined in Section 2. The epicentral distance (Δ) and backazimuth are calculated with respect to the location of the seismic station ANKY.

$\lambda_j \in [23.285, 23.320]$, $j \in [1, 8]$), meaning that all stations are allowed to be placed anywhere within the parameter space. The area defined by the station latitude and longitude boundaries is mainly determined by the overall shape of the island, by trying to cover as much land area as possible and omit water area since only land based three-component seismometers are planned to be deployed at this stage. Moreover, the main road network of the Antikythera island which follows smoother topographic conditions and is expected to make the array deployment easier, should be taken into account.

To address these conditions, we considered a grid with 350 m × 600 m cells, over the area that is defined by the parameter space boundaries (Fig. S3 in the Supplementary material). We then discretised the road network, and if at least one of these points lies within a grid-cell, then a station is allowed to be deployed anywhere within that cell. Grid-cells that lack a road network or those that cover water area are excluded, meaning that our parameter space has in practice an irregular shape, instead of a rectangular shape defined by using just four coordinate pairs. It is worth noting that the above grid is only used to coarsely customise the shape of a valid parameter space and it should not be confused with the optimisation grid. Finally, the inter-station distances should be kept equal as possible, without affecting the overall shape of the array.

3.2 Synthetic seismograms and waveform processing

As already discussed in Section 1, the objective of the new seismic array is to contribute in earthquake location accuracy, where station coverage is sparse. For this reason, array-based seismic event location processes are necessary to be implemented in the current grid search algorithm. One of the most commonly used techniques is the beamforming. This technique is based on the principle that similar to time domain techniques, time differences between coherent signals of the same phase arrival recorded on each array element, will be translated into phase differences in the frequency domain. The beam power is then calculated over a grid within a range of horizontal slowness vectors, and the maximum power indicates the backazimuth and slowness vector of the seismic phase for a given frequency range. A detailed description of seismic array analysis and beamforming techniques can be found in Schweitzer et al. (2009); Rost and Thomas (2002); Douglas (2007).

For the purpose of our study we calculate three-component synthetic waveforms using a discrete wavenumber reflectivity method that computes the stress field radiated by a best-fitting double-couple moment tensor source (Cotton and Coutant, 1997). Our computations are based on a hybrid 1D velocity model superimposing an averaged regional model with seven layers for the crust (Karastathis et al., 2025), on top of the ak135 velocity model (Kennett et al., 1995). Topographic corrections are also applied on the synthetic seismograms based on a digital elevation model (OpenTopography, 2013). Since the completeness magnitude for the area covered by the seismic sources has been estimated to range from 1.5 to 2.0 (Melis et al., 2023), we set the seismic moment in all sources to 2×10^{11} Nm, which corresponds approximately to M_W=1.5.

In order to simulate noise in the synthetic data, a

noise level model was set up based on noise levels of real noise traces from the permanent station ANKY on the island. More specifically, we assumed that ANKY is located at a relatively low noise level site and since no other seismic stations are deployed at Antikythera we identified sites of high noise level due to anthropogenic activity. These are the main village and the port, a heliport and a basketball court at the north-west, and the PANGEA building of the National Observatory of Athens located approximately at the centre of the island. We assumed that noise levels can reach up to 100% increase at the main village, the heliport and the basketball court, and up to 50% increase at the PANGEA building. Since ANKY is deployed close to a road we assumed that the road network should be at the same noise level recorded at ANKY station. Fig. 2 shows the obtained noise level for Antikythera where hot spots are observed at the NW, whereas the noise level at the rest of the island is relatively similar to the noise level of ANKY station.

High-frequency white noise based on the model of Fig. 2 is then added to the seismograms, the mean and trend is removed, and a 5% Hanning taper is applied. A 8-second P-wave window is then selected from the vertical component (Z), and beamforming is applied, in order to determine the backazimuth for each seismic source. The horizontal components are then rotated to radial (R) and transverse (T), in order to separate the S waves into SV and SH, and the beamforming is applied again on the transverse component. Fig. 3 shows a characteristic example of this process for the third seismic source in Tab. 1. The backazimuths associated with the maximum beam power of the P-wave and SH-wave beams determine the overall array-source backazimuth. The epicentral distance is calculated by the P-S differential travel times, and then, the best-fitting depth that minimises the travel time residuals is estimated in one-kilometer increments.

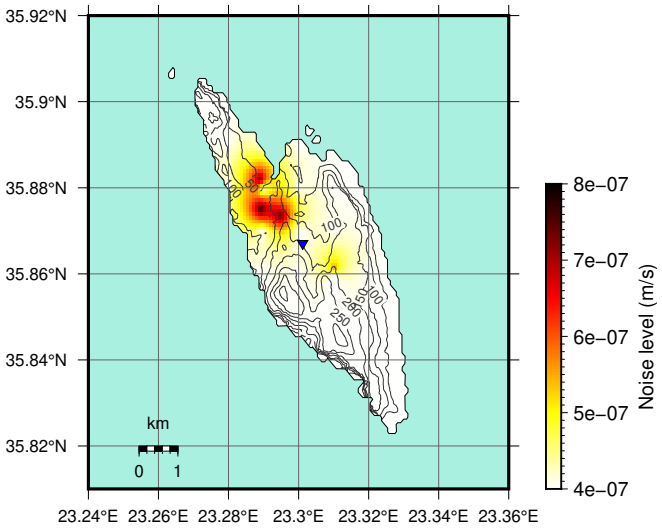

Figure 2 Noise signal amplitude for Antikythera. The black contour lines show the topography, and the blue inverted triangle denotes the location of ANKY seismic station.

3.3 Optimisation strategy

After having set up all the necessary components for the grid search, we implement a global optimisation technique based on the neighbourhood algorithm (Sambridge, 1999). This is an effective and easily adapted algorithm with modular design that has been extensively used to solve a wide range of linear and non-linear, ill-posed, geophysical problems (i.e., Sambridge and Kennett, 2001; Beghein et al., 2002; Vallée et al., 2010; Lentas et al., 2014; Lentas and Harris, 2019).

The neighbourhood algorithm makes use of geometrical constructs known as Voronoi cells (Okabe et al., 1995) during the search of the parameter space, which form nearest neighbour regions defined under a suitable distance norm. Its simplicity is based on the fact that only the calculation of the forward problem at each step is carried out, without the need to determine partial derivatives for each search parameter, making it suitable even for problems where analytical expressions are hard to implement (i.e., Lentas and Harris, 2019). Moreover, only two tuning parameters are required, namely, the number of models generated at each iteration (n_s) and the number of Voronoi cells in which the n_s models are randomly selected (n_r). Even though these parameters are usually determined by trial and error, n_s is typically of the order of twice the number of the parameter space dimension (n_d), whereas n_r lies within the range of 2 and n_s/2.

In order to drive the grid search a user supplied objective function is required, and the goal is to find models which minimise this function. In the current study, we set up our objective function by taking into account three basic criteria: (i) a model (a set of station positions) has to maximise the absolute amplitude of the beam that determines the slowness vector and backazimuth of a seismic source; (ii) a model should lead to minimum error (mislocation) in seismic source location based on the backazimuth obtained from the beamforming, when compared to the location of each seismic source of Fig. S2a in the Supplementary material; (iii) a model should comply with the geometric and geographic constraints mentioned above. Specifically, we define our objective function $f(m)$ for each model (m) as:

$$f(m) = w_1 \frac{1}{k} \sum_k log_2(A^2(m)) + w_2 \frac{1}{k} \sum_k \sqrt{\delta_\Delta^2(m) + \delta_h^2(m)} + w_3 \sigma_i^2(m) + w_4 \frac{n - n_v(m)}{n} \quad (2)$$

where k is the number of seismic sources, A^2 is the RMS absolute power of the beam obtained from both first P and S wave arrivals, δ_Δ is the error in horizontal distance (horizontal mislocation), δ_h is the error in depth (depth difference), σ_i^2 is the variance of the inter-station distances in azimuthal order, n is the total number of stations, n_v is the number of valid stations, namely, those that lie within the yellow tiles of Fig. S3 in the Supplementary material. The parameters w_1, w_2, ..., w_4 are weighting factors, determined by trial and error so

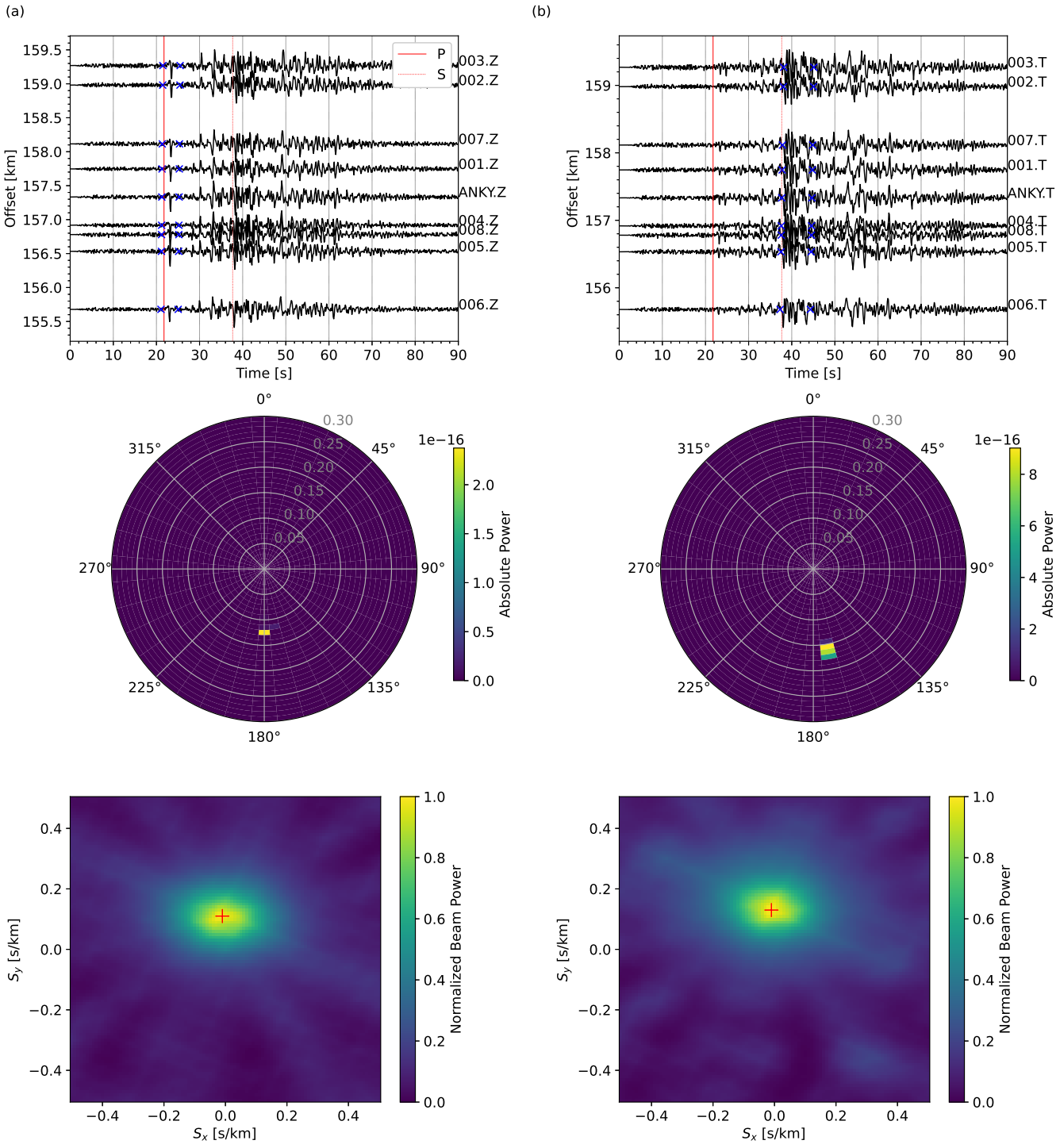

Figure 3 An illustrative example of the beamforming using the P wave on the vertical component (a) and the SH wave on the transverse component (b) for an arbitrary array layout during the optimisation process. The seismic source is located at latitude 34.47°, longitude 23.37°, depth at 41.4 km, and its best-fitting double-couple mechanism has strike 132°, dip 56° and rake 92°. Offset plots of synthetic waveforms with noise added are shown on top, polar plots showing the beam power are shown in the middle, and slowness maps are plotted at the bottom. P-wave and SH-wave time windows used in the beamforming are denoted by the blue crosses. The vertical solid and dotted lines indicate the P-wave and S-wave time arrivals, respectively. The red cross on each slowness map denotes the S_x, S_y pair associated with maximum power.

that each term contributes equally to the objective function. For example, a low value term needs a high weighting factor to counter-balance the effect of a higher value term and vice-versa. If a strong bias is observed as a result of some term, its weighting factor is decreased. On the opposite, a term that seems to have no effect on the optimal model is slightly increased until we start to observe its contribution.

The first term of the objective function is set to maximise the power. The second-base logarithm is used to minimise this term in a linear way as the power increases, since $A^2 < 1$. The second term is associated with the mislocation error, both horizontally and in depth. The rest of the terms in the objective function are associated with the geometric and geographic constraints discussed above. Specifically, as the third term decreases, it ensures that the inter-station distances are kept relatively equal, affecting the overall symmetry of the array. A small value favors a regular shaped array (i.e., circular), whereas, a high value of this term indicates an irregular shaped array. In our study we keep the effect from this term relatively low in order to account for irregular shaped arrays too. Finally, when the number of valid stations n_v increases, the fourth term decreases, until it is vanished when all stations are placed by the algorithm within the yellow tiles of Fig. S3 in the Supplementary material ($n_v = n$).

As seen in Fig. 1 the seismic sources used for the optimisation are scattered across a relatively vast region measuring $3^\circ \times 4^\circ$ with some variability in strike orientation. As a result it is likely that some sources may align with array models during the optimisation which can significantly distort beamforming amplitudes since the signal-to-noise ratio may decrease substantially, especially for P-waves. One could attempt to introduce one more term in the objective function of equation 2 in order to penalise such array configurations during the optimisation process, although this is hard to implement directly. Nevertheless, this is already indirectly implemented since the latter would lead to higher errors in the locations which would yield an overall high value for the objective function. Thus, we rather let the optimisation to determine the optimal array model for the entire set of seismic sources, having in mind that inevitably there might be a few sources which may show higher location errors compared to others.

4 Results

4.1 Parameter settings

Before we obtain the final results using the method developed in Section 3, we had to define the weighting factors for the objective function and the two tuning parameters of the neighbourhood algorithm (see Section 3.3). Since our parameter search problem is based on synthetic data, and hence, it is not possible to define a true model to tune the algorithm based on it, we started by giving values to the weighting parameters so that each term of equation 2 would contribute relatively equally to the final value of the objective function. In other words, the product of the first weight and term yields a value comparable to the product of the second weight and term, and so on, given the overall span of each term during the optimisation. Thus, high weights may not necessarily mean a strong effect and vice-versa (see Tab. 2 for detailed weighting factor values and input parameters used in the optimisation), although the term that controls the number of valid station locations was prioritised in order to ensure that the optimal model will not include stations at the sea. Even though this is a strong constraint that may bias the optimal model up to some degree and prevent the algorithm from identifying better-performing configurations, unfortunately, it is not possible to avoid due to the problem's logistics. The terms of power amplitude and mislocation were given weighting factors to ensure that beam power will increase and location errors will reduce during the optimisation. Finally, the term that monitors the inter-station distances was given a relatively low weight just to ensure that some stations will not collocate.

Regarding the neighbourhood algorithm parameters we started by giving small values for n_s and keeping n_r between 2 and n_s/2. We gradually increased the n_s parameter until we started to observe a stable behaviour of the algorithm and the results were consistent from one test to another. We concluded that robust sampling of the parameter space was achieved by setting n_s = 16 and n_r = 4, after 1500 iterations. Further increasing the n_s parameter did not seem to affect the results. Even though our n_s value is lower than twice the parameter space dimension, we believe that due to the narrow range of the search parameters (see Section 3.1) it is still feasible to adequately sample the parameter space by using such values for n_s and n_r.

4.2 Optimal model

Based on the parameter settings mentioned above, the grid search generated 16 initial samples and 24000 models in total. Fig. S4 in the Supplementary material highlights the ability of the algorithm to sample the parameter space. The concentration of a considerable number of models with low objective function values at different spots in some of the inter-parameter plots may indicate local minima, but the convergence around the optimal model is also very clear.

Fig. 4 shows the evolution of the objective function throughout the optimisation process, as well as other crucial terms of equation 2. The very first model during the grid search showed the highest objective function value (Fig. 4a), since all stations were placed in the centre of the parameter space. As a consequence, such an array has no slowness resolution, leading to the lowest observed beam power and highest mislocation. Moreover, stations that share the same coordinates are penalised and characterised as invalid (Fig. 4b) which increases the objective function value accordingly. A steep decrease in the objective function is observed within the first 80 iterations (∼1300 models, Fig. 4a), followed by some abrupt peaks as the algorithm searched the parameter space, approximately until the 600^{th} iteration (10000 models). It then started to converge around the optimal model at the 1460^{th} iteration. It is worth

Parameter	Value
Number of sources	23
$M_\circ$ (Nm)	2.0×10^{11}
Velocity model (crust)	1D model based on Karastathis et al. (2025)
Velocity model (mantle)	ak135 (Kennett et al., 1995)
Sampling rate (Hz)	8.5
Slowness range (s/km)	±0.3
n_d	16
φ_j [min, max], $j \in$[1, n_d/2]	[35.835, 35.885]
λ_j [min, max], $j \in$[1, n_d/2]	[23.285, 23.320]
Number of iterations	1500
n_s	16
n_r	4
w_1	0.003
w_2	0.020
w_3	0.070
w_4	3.000

Table 2 Table summarising the input, model and weighting parameters used in the optimisation.

noting that as long as stations started to separate within the first few iterations, the mislocation term decreased dramatically (Fig. 4e), even if the beam power still showed large variations (Fig. 4d). As mentioned above a few better array layouts may have been penalised by the algorithm inevitably, since some stations may have been placed outside the yellow tiles of Fig. S3 in the Supplementary material. For example some models produced high beam power values within the first 1200 models (Fig. 4d), but they are associated with high objective function values as a result of the fourth term in equation 2.

Scatter plots among different terms controlling the objective function (Fig. 5) revealed that seismic array layouts with similar inter-station distances (low variance values) usually tend to lead to lower mislocation (Fig. 5a). The same is not necessarily true when studying the mislocation against the maximum beam power (Fig. 5b), where even though high beam power usually yields lower mislocation, nevertheless, some exceptions are evident. A clear trend also found when comparing the beam power against the shape of the array, where the highest beam power values are associated with similar inter-station distance array layouts. It is also very clear how the very first model during the grid search (all stations at the same location), showing maximum objective function value, separates from the rest of the models.

Fig. 6a presents the optimal seismic array layout that maximised the beam power, and minimised the horizontal and depth mislocation for the seismic sources presented in Section 2 (see also Tab. 1). The eight stations have been positioned in a relatively irregular layout, with all newly added stations falling within the yellow tiles which mark the areas that stations are allowed to be deployed. The aperture of the array is approximately 4 km in N-S orientation with centre-to-station distances ranging from 120 m to 2 km approximately, showing that the final layout was controlled mainly by the last term of equation 2 and the two terms associated with the actual location problem (beam power and mislocation terms). Other geometrical constraints (inter-station distances) do not seem to have affected dramatically the result. The detailed coordinates of the stations are summarised in Tab. 3. The newly added stations are placed away from sources of high noise levels, given the spatial constraints, but some variation in the elevation is inevitable since the topographic changes on the island are dramatic. It is worth noting that incorporating the elevation model into the synthetics prevented the selection of stations located near the highest topographic peak ($>$ 300 m) in the southwestern part of the island. The theoretical transfer function of the obtained seismic array (Fig. 6) shows a circular peak following the array layout, with minimal side lobes around it (up to 3 Hz) indicating high slowness resolution, and only becoming stronger in higher frequencies as expected.

The latter is also obvious when studying the performance of the optimal array layout in its ability to obtain the backazimuth for each seismic source through beamforming. All seismic sources showed small deviations from their true backazimuth values (Fig. 7), usually within 2.5°, with the only outlier being the source at the longest distance to the array (source 10, in Tab. 1) which showed a backazimuth difference of 5°. This represents a pure thrust faulting, shallow dipping to the NE seismic source, oriented in NW-SE direction. Other shallow dipping seismic sources also showed large mislocation errors (i.e., sources 7 and 18) most likely associated with their radiation patterns which yield lower $M_{r\theta}$ and $M_{r\phi}$ moment tensor components.

Fig. 8 shows the co-array geometry of the optimal array layout and its phase response to an incoming wavefront from SE assuming a plane-wave. The co-array locations are calculated as the difference of position vectors for each possible pair of sensors, showing waveform coherence and time shifts between sensors expressed as phase shifts. The layout of the array yields no significant gaps in the co-array and coherent banded patterns of phase shifts can be observed up to 2.0 Hz. In the 2.0 Hz - 4.0 Hz frequency band the effect of noise is stronger which inevitably affects waveform semblance.

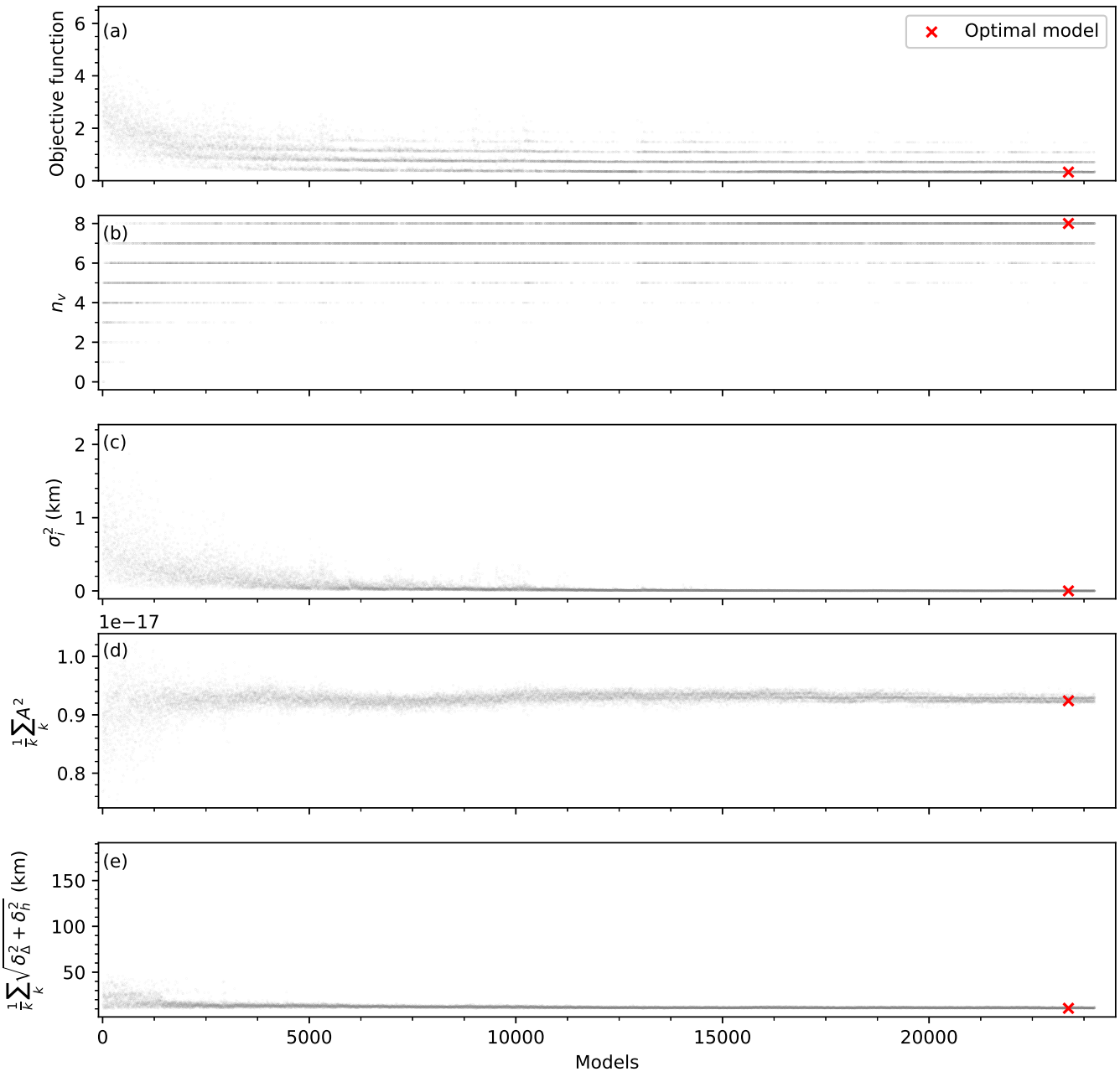

Figure 4 Scatter plots showing the evolution of the objective function (a), and its terms (see also equation 2) throughout the optimisation process, namely, the number of valid stations (n_v) (b), geospatial constraints ($\sigma_i^2(m)$) (c), beam power ($\frac{1}{k}\sum_k log_2(A^2(m))$) (d), and mislocation ($\frac{1}{k}\sum_k \sqrt{\delta_\Delta^2(m)+\delta_h^2(m)}$) (e). For a detailed description of each term please refer to Section 3.3. The horizontal axis represents the index of each model and the red cross indicates the optimal model.

The orientation of alternating colour bands indicate that the wave approaches from the correct direction.

4.3 Seismic array layout effect

The optimal seismic array obtained in Section 4.2 was tested against two regular layout arrays, namely, a cross-shaped array, and a rectangular array, with both having nine elements in total (including ANKY permanent station). For a number of reasons, namely, the irregular shape of the island and its overall small dimensions, the symmetry of these arrays and the fact that the location of the permanent station is not allowed to change, both of these arrays have limited options on where to be deployed. The most reasonable option seems to have ANKY station in the centre of each array (Fig. 9). As a result they both have a smaller aperture (3 km) compared to our optimal array. Moreover, some stations had to be positioned slightly off the yellow tiles in each case, to ensure symmetry across ANKY station, which in reality would be unreasonable taking into account the steep cliffs of the island which would make deployment of the sensors impossible.

Figs S5 and S6 in the Supplementary material show their theoretical transfer functions, respectively. The cross-shaped seismic array is symmetrical, diamond-shaped, with a wide peak in the lower frequencies (0.5 Hz - 1.0 Hz). The main peak becomes sharper in higher

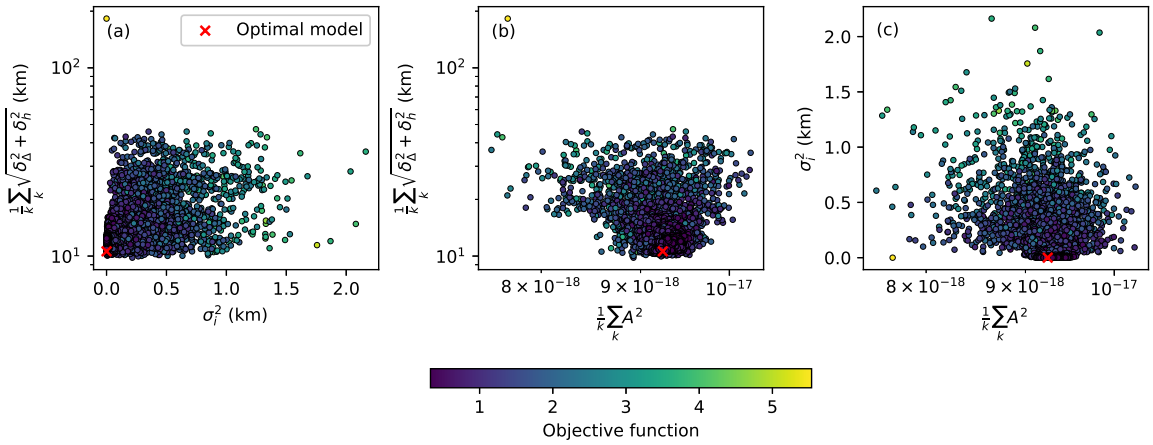

Figure 5 Scatter plots presenting the relationships between different terms of the objective function, namely, the mislocation term ($\frac{1}{k}\sum_k \sqrt{\delta_\Delta^2(m)+\delta_h^2(m)}$) against the geospatial constraints ($\frac{1}{2}(\sigma_c^2(m)+\sigma_i^2(m))$) (a), the mislocation term ($\frac{1}{k}\sum_k \sqrt{\delta_\Delta^2(m)+\delta_h^2(m)}$) versus the beam power ($\frac{1}{k}\sum_k log_2(A^2(m))$) (b), and the geospatial constraints ($\sigma_i^2(m)$) against the beam power ($\frac{1}{k}\sum_k log_2(A^2(m))$) (c), colour-coded by the objective function. For a detailed description of each term please refer to equation 2 in Section 3.3.

Station code	Latitude (°)	Longitude (°)	Elevation (m)	Centre-to-station distance (m)	Azimuth (°)
001	35.871	23.307	83	612.8	58.3
002	35.882	23.310	183	1732.5	25.4
003	35.884	23.296	56	1869.5	345.0
004	35.863	23.295	197	836.0	228.5
005	35.860	23.304	159	923.1	168.9
006	35.852	23.294	207	1934.4	201.6
007	35.871	23.291	66	982.0	287.7
008	35.862	23.317	153	1505.0	114.2
ANKY	35.867	23.301	143	127.7	206.2

Table 3 Table summarising the locations of the optimal array obtained in the current study. The elevation is determined by the digital elevation model downloaded from the OpenTopography web services (https://opentopography.org/, OpenTopography, 2013). Azimuth values refer to the centre of the array.

frequencies, but a weak cross-shaped side lobe between 1.0 Hz and 3.0 Hz starts to emerge, as well as a few strong side lobes in the 3.0 Hz - 5.0 Hz frequency band (Fig. S5 in the Supplementary material). The rectangular array shows a somewhat elliptical wide peak with the major axis oriented horizontally in the 0.5 Hz - 1.0 Hz frequency band, and progressively sharper main peaks with frequency. Compared with the cross-shaped array, the rectangular array shows many more strong side lobes in frequencies above 1.0 Hz (Fig. S6 in the Supplementary material). Even though all three transfer functions show relatively similar resolution, our obtained array layout is better in the aspect that it is showing weaker side lobes compared to the regular shaped array layouts, as well as slightly sharper peaks in all three frequency bands (Fig. 6).

Figs S7 and S8 in the Supplementary material present the co-array coherence and phase response to the same wavefront as discussed in Fig. 8 for the two regular shaped arrays. Both arrays show some gap in the middle in comparison with our optimal array and they cover a noticeably narrower area since some co-array locations coincide as a result of symmetry. Nevertheless, they both sense the correct direction of the incoming wavefront. Surprisingly, the cross-shaped array shows low coherency for the closest to the source sensors in the lower frequency band, whereas the rectangular array shows suspiciously high coherency in the highest frequency band given that noise effects are stronger in higher frequencies. This may be an indication that the observed waveform semblance is just a coincidence.

All three arrays achieved almost the same levels of maximum beam power, (Fig. 10). The backazimuth is overall resolved better by the optimal array compared to the regular arrays, which only showed equal or slightly better results in a just few cases. Nevertheless, both regular arrays are hard to implement on the Antikythera island due to geospatial constraints that have been taken into account in the determination of the optimal array layout.

5 Discussion and Conclusions

In this study we obtained the optimal layout for a small-aperture seismic array to be deployed at the Antikythera

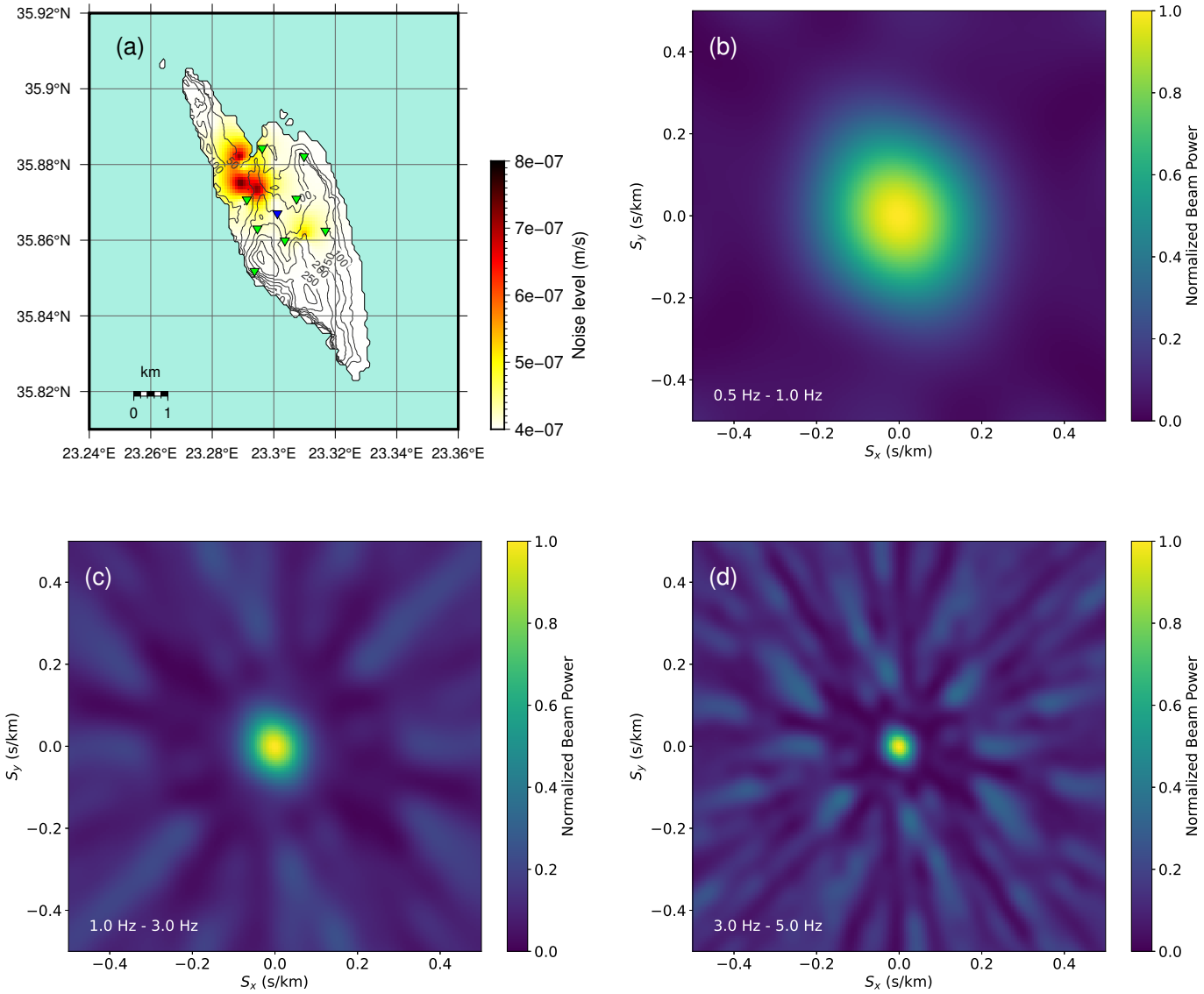

Figure 6 A map of the Antikythera island showing the locations of the optimal array layout (a). The blue inverse triangle shows the location of ANKY station, and the green inverse triangles represent the locations of the eight stations obtained through the optimisation process. Black contour lines represent elevation in metres. The noise level is shown in the background (see colour-scale). The array transfer function of the optimal array is also plotted for different frequency bands, namely, 0.5 Hz - 1.0 Hz (b), 1.0 Hz - 3.0 Hz (c) and 3.0 Hz - 5.0 Hz (d).

island, in order to enhance the detection capability and location accuracy of the Hellenic Unified Seismic Network in Greece (National Observatory of Athens, Institute of Geodynamics, Athens, 1975), for the seismic activity observed at the west part of the Hellenic Subduction Zone. For this purpose, we neither restrict to regular-shaped seismic array designs, nor we followed theoretical array transfer function calculations that may have ignored geospatial and/or logistics constraints, as well as the ability to resolve the slowness vector of real case seismic events on a study area. Instead of deploying possible array designs on the site, where one would have to test and adjust the layout based on real earthquake recordings (Mykkeltveit, 1985), our approach followed a flexible, time saving and cost effective method based on maximising the beam power and minimising the location error of a synthetic dataset through a global optimisation grid search technique similar to Karamzadeh et al. (2018). Nevertheless, our implementation also takes into account geospatial constraints that may be necessary in some sites such as islands and/or areas with vast topographic variations.

The simple use of the array transfer function to design a seismic array, although based on wave propagation principles, only controls the inter-station distances and the overall aperture of the array on a theoretical manner. For example, the inter-station distances shall be small enough to prevent spatial aliasing and ensure high signal coherence between the station elements of the array, but the station separation shall stay large enough to suppress seismic noise correlation (Mykkeltveit and Bungum, 1984). Nevertheless, the array layout can only be determined by trial and error and one would have to make an educated guess on the optimal layout, not to mention that seismic source directivity effects cannot be implemented on such a design process.

On the contrary, by setting up a synthetic, yet realis-

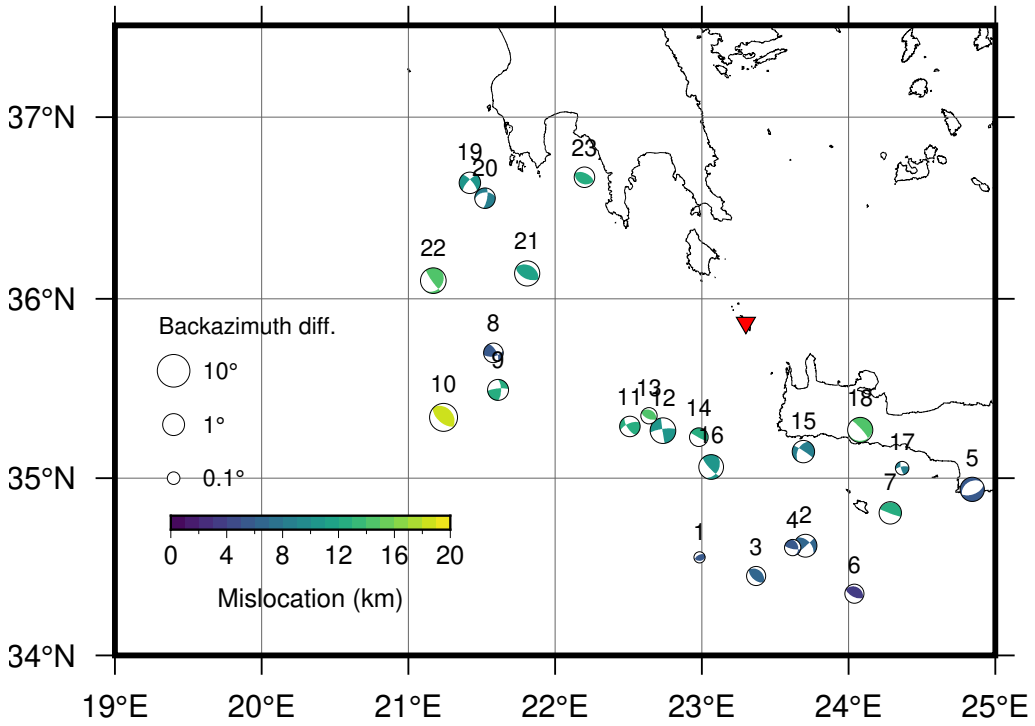

Figure 7 Maps showing the 23 seismic sources expressed by their best-fitting double-couple mechanisms used in the optimisation process, colour-coded by the horizontal and vertical mislocation. The backazimuth difference is proportional to the size of the beachballs. Source index numbers according to Tab. 1 appear on top of each beachball.

tic, dataset we let a grid search algorithm to freely test any possible array layout, and by setting up an objective function based on certain criteria, we concluded on the optimal layout for our given design objectives. More specifically, the array at the Antikythera island should be able to detect and achieve a high beam power for seismic events mainly at a distance up to 150 km approximately, covering a wide range of azimuth and a vast variety of earthquake mechanisms from pure normal to oblique type and thrust type mechanisms (see for example Fig. S1 in the Supplementary material). In addition, a number of geospatial characteristics imposed constraints on the final design. The strongest constraint is the elongated shape and overall small size of the island which only favors the deployment of small aperture arrays, either of square to circular shape on the centre of the island, or line arrays along its major axis. Nevertheless, one should also take into account topographic constraints and a limited road network as a result of a few NNW-SSE oriented normal faults (Veliz-Borel et al., 2022).

The proposed seismic array of this study (Fig. 6a) follows an irregular layout with an aperture of approximately 4 km. The shape and aperture of the array were primarily controlled by the frequency-wavenumber characteristics of the wavefield produced by the synthetic dataset and the constraint for the positioning of the stations in easily accessible locations after taking into account a basic noise level model for the Antikythera island and topographic conditions. The array's shape ensures good sensitivity for a range of azimuths (150°-300°), and the short inter-station distances are expected to favor a high degree of signal coherency and suppress noise levels under real conditions. This is of high significance if one also considers the topographic variations on the island which can introduce additional phase shifts among the different array stations (Ødegaard et al., 1990; Schweitzer, 1998). The overall aperture of the obtained array is expected to allow for seismic event detection up to 150 km. For example, NORESS array with a 3 km aperture is able to detect regional events within the 0.5 Hz - 10 Hz frequency range (Kværna, 1989). Moreover, an experimental, 750 m aperture array in south-western Peloponnese had successfully detected and located seismic events in epicentral distances up to 100 km (Bocchini et al., 2018). Based on the current study we are aiming to complement the event detection capabilities of the seismological network of the Geodynamics Institute (National Observatory of Athens, Institute of Geodynamics, Athens, 1975), in an area with sparse seismic station coverage yielding earthquake locations characterised by high azimuthal gaps. Alternatively, instead of using only traditional beamforming methods, more advanced array-based techniques (Gibbons and Ringdal, 2006) to detect seismic events could also be applied (i.e., Pirli et al., 2010, 2013).

It is in general preferable that all array stations should be deployed on the same geological background, since any heterogeneities will introduce phase shifts among the recordings of the wavefront by the different array elements, and reduce their degree of coherence (Rost and Thomas, 2002; Pirli et al., 2006). The geological conditions on the island of Antikythera are not too complex overall, with very thin Neogene sediments (sandy marls and clay) covering limestones and flysch of Mesozoic age (Lyberis et al., 1982). Nevertheless, this constraint was not taken into account in our objective func-

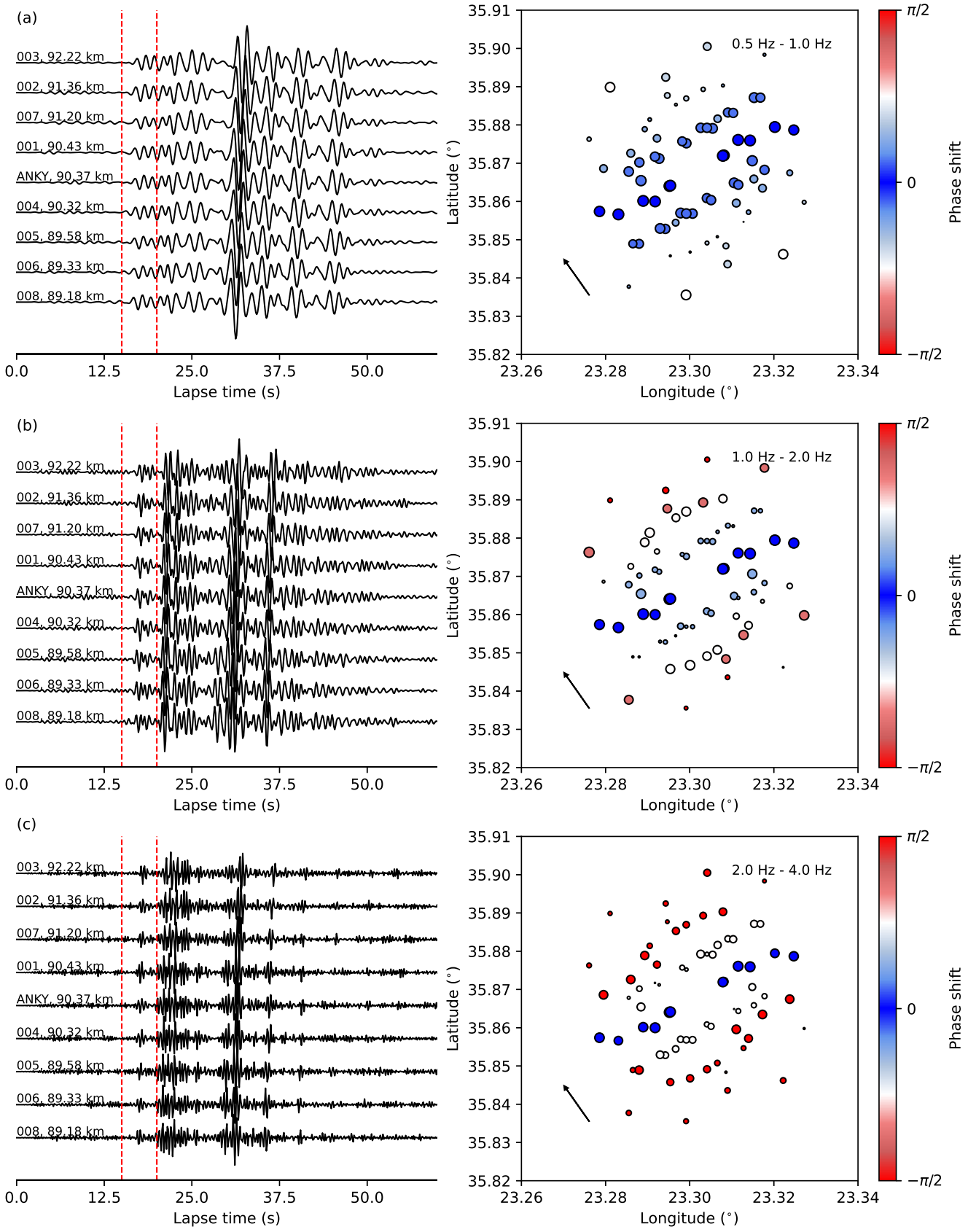

Figure 8 Co-array analysis of the optimal array layout shown in Fig. 6 for different narrow frequency bands, namely, 0.5 Hz - 1.0 Hz (a), 1.0 Hz - 2.0 Hz (b) and 2.0 Hz - 4.0 Hz (c). Synthetic seismograms of a seismic source from a backazimuth of 147° are shown in the left hand side ordered by epicentral distance (bottom to top). Time delay measurements were made in data segments denoted by the red vertical lines. The time delays between all the array element pairs are expressed in phase shifts (see colour-scale) on the maps in the right hand side. The circle size is proportional to signal coherence. The black arrow represents the direction of propagation of the incoming seismic wavefront.

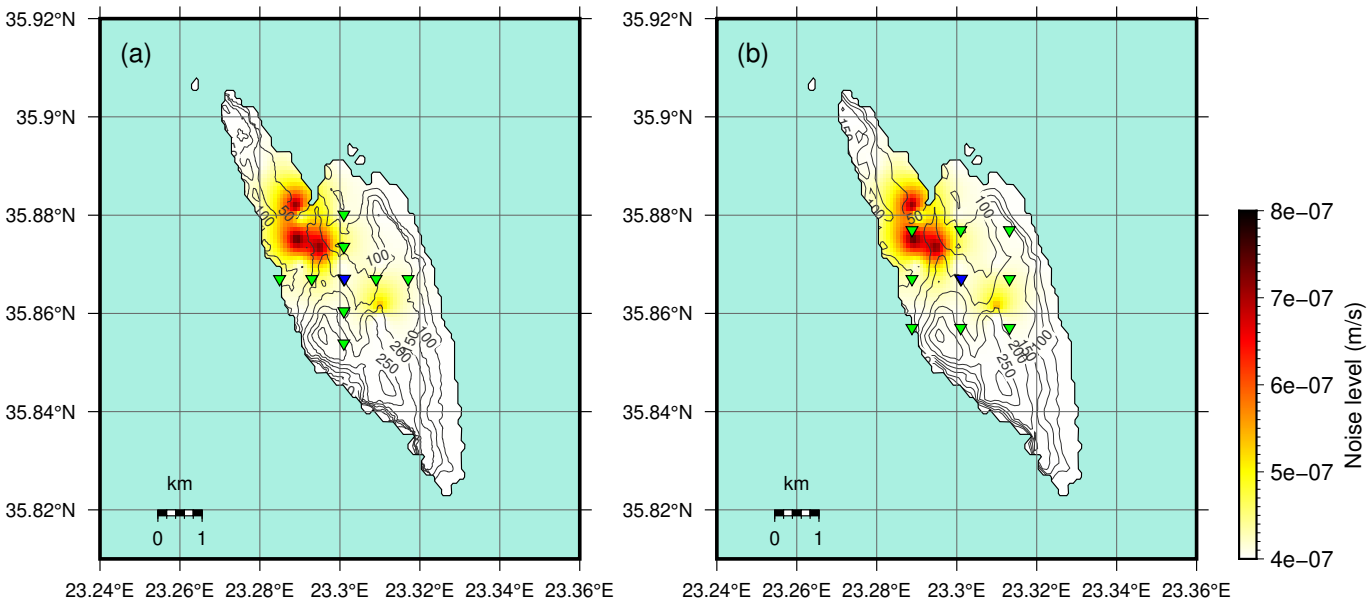

Figure 9 Same as in Fig. 6a, but for a cross-shaped array (a) and a rectangular type array (b).

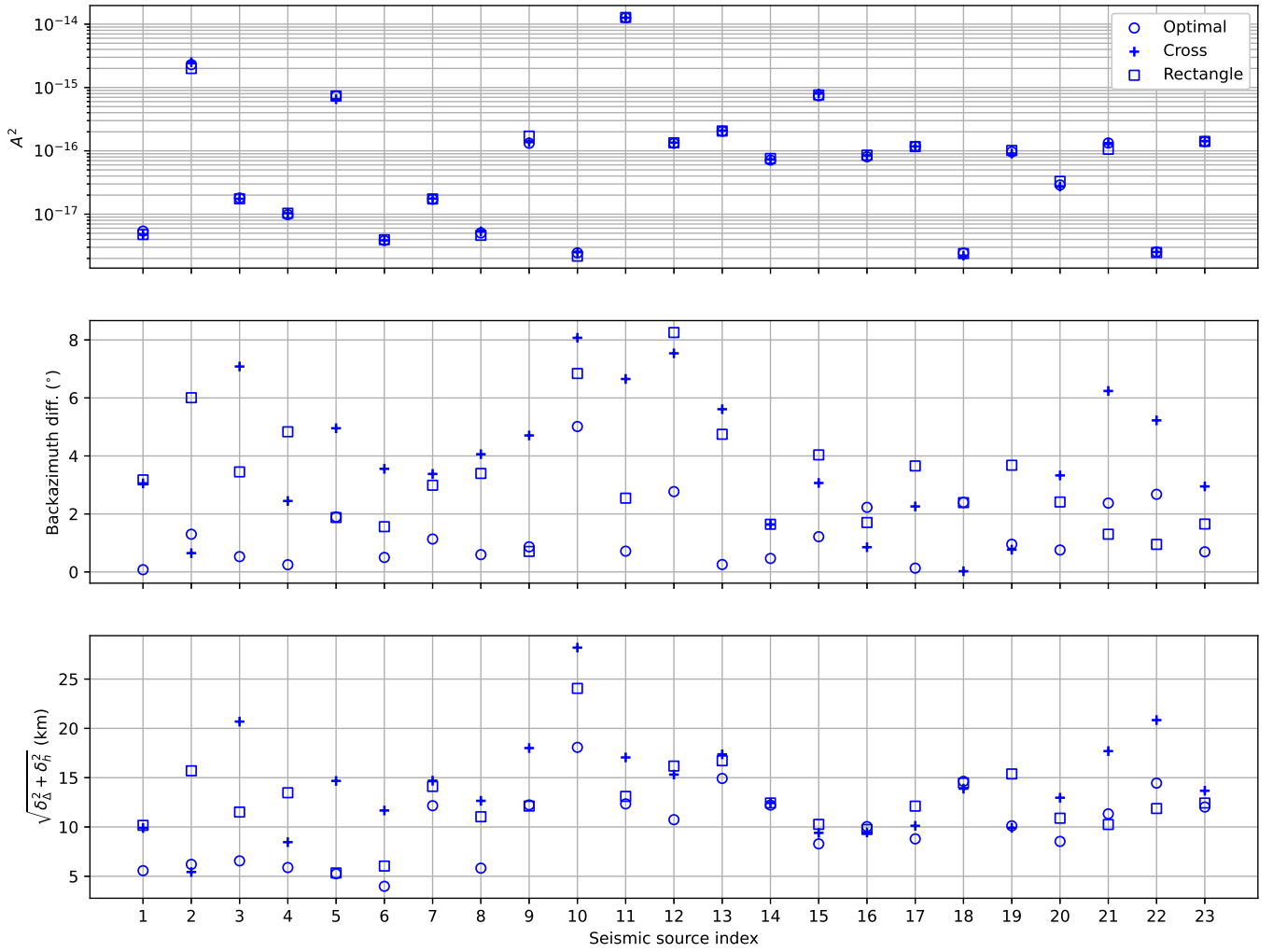

Figure 10 Scatter plots summarising the beam power (top), backazimuth difference (absolute values) with respect to true backazimuth referring to the location of ANKY permanent station (middle), and mislocation (bottom) for each seismic source, obtained by the use of the optimal array and those presented in Fig. 9.

tion since it would considerably reduce the space allowed for station installations with respect to the overall dimensions of the island. Slight adjustments to the final station locations may be necessary (i.e., up to 50 m)

in the field in order to ensure homogeneous geological conditions and/or reducing elevation differences, without affecting too much the slowness resolution of the array.

The seismic array discussed in this study is consisted of a large number of stations, nine in total, given its aperture. This was done in order to achieve a high beam power since the larger number of stations, the stronger wavenumber filtering is achieved by the array, by suppressing energy with different slowness (i.e., noise) that crosses the array simultaneously (Schweitzer and Kværna, 2002). Nevertheless, there is a tradeoff between the number of stations and inter-station distances, and hence, the aperture of a seismic array given that spatial constraints may apply. The latter has an effect on the wavelength that can be resolved by an array. For example, the optimal array obtained in this study with an aperture of 4 km, is well-suited to resolve seismic waves in the 0.5 Hz - 3.0 Hz frequency band for seismic waves traveling in the crust ($V_P \sim 6.5$ km/s, $V_S \sim 3.7$ km/s) and upper mantle ($V_P \sim 8.2$ km/s, $V_S \sim 4.5$ km/s, Kennett et al., 1995).

Finally, we tested two regular shape and purely symmetrical arrays, namely, a cross-shaped array and a rectangular array, against the proposed array layout in this study. We found that overall the latter performed better than the regular shape arrays. Karamzadeh et al. (2018) when carrying out a similar experiment reported that a uniform array geometry can perform better in terms of the array beam power, which has not been clearly observed in our case. A possible explanation may be due to differences in the noise level added to the synthetic waveforms. Our optimal array showed small-scale but clear improvement in backazimuth and location errors compared to the regular shape arrays, which can be explained by the fact that spatial constraints were applied during the optimisation. If no such constraints were taken into consideration a different layout may have emerged leading to significantly improved location estimates. Unfortunately, in real-world applications, especially in oceanic environments where seismic station deployment is limited on small remote islands these constraints cannot be neglected. Here we presented a possible framework of implementing spatial constraints in seismic array design optimisations and the fact that the proposed array determined by a grid search algorithm performed slightly better compared to regular shape arrays, makes us confident to believe that it will perform adequately under real-life conditions.

Acknowledgements

The authors would like to thank the Editor Dr. Stephen Hicks and the Reviewers: one anonymous Reviewer and Dr. Roberto Cabieces Díaz, whose comments helped to improve the manuscript.

Data and code availability

The moment tensor catalogue used in this study was compiled using the Global CMT catalogue (GCMT, Dziewonski et al., 1981; Ekström et al., 2012, https://www.globalcmt.org/, database last accessed on December 2024) and the NOA moment tensor catalogue (Triantafyllis et al., 2021, https://bbnet.gein.noa.gr/HL/seismicity/mts, database last accessed on December 2024). Earthquake mechanism clustering was carried out using the FMC package (Álvarez Gómez, 2019, https://github.com/Jose-Alvarez/FMC). Synthetic waveforms computed using the AXITRA Fortran 90/95 code (https://github.com/coutanto/axitra). The waveform and beamforming analysis was carried out using ObsPy (Beyreuther et al., 2010, https://docs.obspy.org/). This study makes use of the computer package neighbourhood algorithm (Sambridge, 1999) which was made available with support from the AuScope inversion laboratory (ilab, https://iearth.edu.au/codes/NA/). The code designed specifically for this paper can be accessed through a public data repository (https://zenodo.org/records/18195312). Figures created using the matplotlib library (Hunter, 2007, https://matplotlib.org/) and Generic Mapping Tools (GMT, Wessel et al., 2019, https://www.generic-mapping-tools.org/).

Competing interests

The authors have no competing interests.

References

Ajo-Franklin, J. B., Dou, S., Lindsey, N. J., Monga, I., Tracy, C., Robertson, M., Rodriguez Tribaldos, V., Ulrich, C., Freifeld, B., Daley, T., and Li, X. Distributed Acoustic Sensing Using Dark Fiber for Near-Surface Characterization and Broadband Seismic Event Detection. *Scientific Reports*, 9(1), Feb. 2019. doi: 10.1038/s41598-018-36675-8.

Almendros, J., Abella, R., Mora, M. M., and Lesage, P. Array analysis of the seismic wavefield of long-period events and volcanic tremor at Arenal volcano, Costa Rica. *Journal of Geophysical Research: Solid Earth*, 119(7):5536–5559, July 2014. doi: 10.1002/2013jb010628.

Beghein, C., Resovsky, J. S., and Trampert, J. P and S tomography using normal-mode and surface waves data with a neighbourhood algorithm: P and S tomography with a neighbourhood algorithm. *Geophysical Journal International*, 149(3):646–658, May 2002. doi: 10.1046/j.1365-246x.2002.01684.x.

Beyreuther, M., Barsch, R., Krischer, L., Megies, T., Behr, Y., and Wassermann, J. ObsPy: A Python Toolbox for Seismology. *Seismological Research Letters*, 81(3):530–533, May 2010. doi: 10.1785/gssrl.81.3.530.

Bocchini, G. M., Karastathis, V., Voulgaris, N., Mouzakiotis, A., Papadopoulos, G., Gika, F., Liakopoulos, S., Tselentis, A., and Lantzourakis, P. Enhancing routine seismicity monitoring by using a small aperture seismic array, results from the experimental stage of the Pylos array (Western Peloponnese, Greece). 36^{th} ESC General Assembly, Valletta, Malta. 2018.

Bungum, H., Husebye, E. S., and Ringdal, F. The NORSAR Array and Preliminary Results of Data Analysis. *Geophysical Journal International*, 25(1–3):115–126, Dec. 1971. doi: 10.1111/j.1365-246x.1971.tb02334.x.

Cabieces, R., Krüger, F., Garcia-Yeguas, A., Villaseñor, A., Buforn, E., Pazos, A., Olivar-Castaño, A., and Barco, J. Slowness vector estimation over large-aperture sparse arrays with the Continuous Wavelet Transform (CWT): application to Ocean Bot-

tom Seismometers. *Geophysical Journal International*, 223(3): 1919–1934, Sept. 2020. doi: 10.1093/gji/ggaa427.

Cabieces, R., Harris, K., Ferreira, A. M. G., Tsekhmistrenko, M., Hicks, S. P., Krüger, F., Geissler, W. H., Hannemann, K., and Schmidt-Aursch, M. C. Clock drift corrections for large aperture ocean bottom seismometer arrays: application to the UPFLOW array in the mid-Atlantic Ocean. *Geophysical Journal International*, 239(3):1709–1728, Sept. 2024. doi: 10.1093/gji/ggae354.

Capon, J. Investigation of long-period noise at the large aperture seismic array. *Journal of Geophysical Research*, 74(12): 3182–3194, June 1969. doi: 10.1029/jb074i012p03182.

Capon, J., Greenfield, R., and Kolker, R. Multidimensional maximum-likelihood processing of a large aperture seismic array. *Proceedings of the IEEE*, 55(2):192–211, 1967. doi: 10.1109/proc.1967.5439.

Cessaro, R. K. and Chan, W. W. Wide-angle triangulation array study of simultaneous primary microseism sources. *Journal of Geophysical Research: Solid Earth*, 94(B11):15555–15563, Nov. 1989. doi: 10.1029/jb094ib11p15555.

Cotton, F. and Coutant, O. Dynamic stress variations due to shear faults in a plane-layered medium. *Geophysical Journal International*, 128(3):676–688, Mar. 1997. doi: 10.1111/j.1365-246x.1997.tb05328.x.

DeMets, C., Gordon, R. G., Argus, D. F., and Stein, S. Current plate motions. *Geophysical Journal International*, 101(2):425–478, May 1990. doi: 10.1111/j.1365-246x.1990.tb06579.x.

Douglas, A. Forensic seismology revisited. *Surveys in Geophysics*, 28(1):1–31, Jan. 2007. doi: 10.1007/s10712-007-9018-7.

Dziewonski, A. M., Chou, T., and Woodhouse, J. H. Determination of earthquake source parameters from waveform data for studies of global and regional seismicity. *Journal of Geophysical Research: Solid Earth*, 86(B4):2825–2852, Apr. 1981. doi: 10.1029/jb086ib04p02825.

Eilon, Z. C., Gaherty, J. B., Zhang, L., Russell, J., McPeak, S., Phillips, J., Forsyth, D. W., and Ekström, G. The Pacific OBS Research into Convecting Asthenosphere (ORCA) Experiment. *Seismological Research Letters*, 93(1):477–493, Oct. 2021. doi: 10.1785/0220210173.

Ekström, G., Nettles, M., and Dziewoński, A. The global CMT project 2004–2010: Centroid-moment tensors for 13,017 earthquakes. *Physics of the Earth and Planetary Interiors*, 200–201:1–9, June 2012. doi: 10.1016/j.pepi.2012.04.002.

Frankel, A., Hough, S., Friberg, P., and Busby, R. Observations of Loma Prieta aftershocks from a dense array in Sunnyvale, California. *Bulletin of the Seismological Society of America*, 81(5): 1900–1922, Oct. 1991. doi: 10.1785/bssa0810051900.

Friedrich, A., Krüger, F., and Klinge, K. Ocean-generated microseismic noise located with the Gräfenberg array. *Journal of Seismology*, 2(1):47–64, Mar. 1998. doi: 10.1023/a:1009788904007.

Furumoto, M., Kunitomo, T., Inoue, H., Yamada, I., Yamaoka, K., Ikami, A., and Fukao, Y. Twin sources of high-frequency volcanic tremor of Izu-Oshima Volcano, Japan. *Geophysical Research Letters*, 17(1):25–27, Jan. 1990. doi: 10.1029/gl017i001p00025.

Gibbons, S. J. The Applicability of Incoherent Array Processing to IMS Seismic Arrays. *Pure and Applied Geophysics*, 171(3–5): 377–394, Oct. 2012. doi: 10.1007/s00024-012-0613-2.

Gibbons, S. J. and Ringdal, F. The detection of low magnitude seismic events using array-based waveform correlation. *Geophysical Journal International*, 165(1):149–166, Apr. 2006. doi: 10.1111/j.1365-246x.2006.02865.x.

Gibbons, S. J., Kværna, T., and Mykkeltveit, S. Could the IMS Infrasound Stations Support a Global Network of Small Aperture Seismic Arrays? *Seismological Research Letters*, 86(4): 1148–1159, June 2015. doi: 10.1785/0220150068.

Gibbons, S. J., Näsholm, S. P., Ruigrok, E., and Kværna, T. Improving slowness estimate stability and visualization using limited sensor pair correlation on seismic arrays. *Geophysical Journal International*, 213(1):447–460, Dec. 2017. doi: 10.1093/gji/ggx550.

Goldstein, P. and Chouet, B. Array measurements and modeling of sources of shallow volcanic tremor at Kilauea Volcano, Hawaii. *Journal of Geophysical Research: Solid Earth*, 99(B2):2637–2652, Feb. 1994. doi: 10.1029/93jb02639.

Haak, H., Mykkeltveit, S., and Dahlman, O. *Nuclear Test Ban*. Springer Netherlands, 2009. doi: 10.1007/978-1-4020-6885-0.

Hata, M., Nishimura, T., Matsushima, T., Kozono, T., Nagatsuma, T., Murata, K. T., Kikuta, K., Muramatsu, D., and Nakahara, H. Volcanic tremor associated with successive gas emission activity at a boiling pool: Analyses of seismic array and visible image data recorded at Iwo-Yama in Kirishima Volcanic complex, Japan. *Journal of Volcanology and Geothermal Research*, 455: 108212, Nov. 2024. doi: 10.1016/j.jvolgeores.2024.108212.

Hudson, T. S., Baird, A. F., Kendall, J. M., Kufner, S. K., Brisbourne, A. M., Smith, A. M., Butcher, A., Chalari, A., and Clarke, A. Distributed Acoustic Sensing (DAS) for Natural Microseismicity Studies: A Case Study From Antarctica. *Journal of Geophysical Research: Solid Earth*, 126(7), July 2021. doi: 10.1029/2020jb021493.

Hunter, J. D. Matplotlib: A 2D Graphics Environment. *Computing in Science & Engineering*, 9(3):90–95, 2007. doi: 10.1109/mcse.2007.55.

Karamzadeh, N., Heimann, S., Dahm, T., and Krüger, F. Application based seismological array design by seismicity scenario modelling. *Geophysical Journal International*, 216(3):1711–1727, Dec. 2018. doi: 10.1093/gji/ggy523.

Karastathis, V. K., Drakatos, G., Mouzakiotis, E., Sboras, S., Evangelides, C., Daskalaki, E., Lantzourakis, P., Boukouras, K., Fragouli, K., and Chalaris, T. Daily monitoring and analysis of the seismicity in concession area BLOCK 10. Technical report, Institute of Geodynamics, National Observatory of Athens, 2025.

Kaverina, A. N., Lander, A. V., and Prozorov, A. G. Global Creepex Distribution and Its Relation to Earthquake-Source Geometry and Tectonic Origin. *Geophysical Journal International*, 125(1): 249–265, Apr. 1996. doi: 10.1111/j.1365-246x.1996.tb06549.x.

Kennett, B. L. N., Engdahl, E. R., and Buland, R. Constraints on seismic velocities in the Earth from traveltimes. *Geophysical Journal International*, 122(1):108–124, July 1995. doi: 10.1111/j.1365-246x.1995.tb03540.x.

Klaasen, S., Paitz, P., Lindner, N., Dettmer, J., and Fichtner, A. Distributed Acoustic Sensing in Volcano-Glacial Environments—Mount Meager, British Columbia. *Journal of Geophysical Research: Solid Earth*, 126(11), Nov. 2021. doi: 10.1029/2021jb022358.

Kværna, T. On exploitation of small-aperture NORESS type arrays for enhanced P-wave detectability. *Bulletin of the Seismological Society of America*, 79(3):888–900, 06 1989. doi: 10.1785/BSSA0790030888.

Kværna, T. and Ringdal, F. Stability of various f-k estimation techniques. 1986. doi: 10.21348/P.1986.0001.

Kværna, T. and Ringdal, F. Detection Capability of the Seismic Network of the International Monitoring System for the Comprehensive Nuclear-Test-Ban Treaty. *Bulletin of the Seismological Society of America*, 103(2A):759–772, Mar. 2013. doi: 10.1785/0120120248.

Kværna, T., Ringdal, F., Schweitzer, J., and Taylor, L. Optimized Seismic Threshold Monitoring - Part 1: Regional Processing.

Pure and Applied Geophysics, 159(5):969–987, Mar. 2002. doi: 10.1007/s00024-002-8668-0.

Kværna, T., Gibbons, S. J., and Näsholm, S. P. CTBT seismic monitoring using coherent and incoherent array processing. *Journal of Seismology*, 25(5):1189–1207, July 2021. doi: 10.1007/s10950-021-10026-z.

La Rocca, M., Galluzzo, D., Malone, S., McCausland, W., Saccorotti, G., and Del Pezzo, E. Testing Small-Aperture Array Analysis on Well-Located Earthquakes, and Application to the Location of Deep Tremor. *Bulletin of the Seismological Society of America*, 98(2):620–635, Apr. 2008. doi: 10.1785/0120060185.

Lentas, K. and Harris, J. Enhanced performance of ISC focal mechanism computations as a result of automatic first-motion polarity picking optimization. *Journal of Seismology*, 23(5): 1141–1159, Sept. 2019. doi: 10.1007/s10950-019-09862-x.

Lentas, K., Ferreira, A., Clévédé, E., and Roch, J. Source models of great earthquakes from ultra low-frequency normal mode data. *Physics of the Earth and Planetary Interiors*, 233:41–67, Aug. 2014. doi: 10.1016/j.pepi.2014.05.011.

Lentas, K., Bowden, D., Melis, N., Fichtner, A., Koroni, M., Smolinski, K., Bogris, A., Nikas, T., Simos, C., and Simos, I. Earthquake location based on Distributed Acoustic Sensing (DAS) as a seismic array. *Physics of the Earth and Planetary Interiors*, 344: 107109, Nov. 2023. doi: 10.1016/j.pepi.2023.107109.

Lindsey, N. J., Martin, E. R., Dreger, D. S., Freifeld, B., Cole, S., James, S. R., Biondi, B. L., and Ajo-Franklin, J. B. Fiber-Optic Network Observations of Earthquake Wavefields. *Geophysical Research Letters*, 44(23), Dec. 2017. doi: 10.1002/2017gl075722.

Lindsey, N. J., Rademacher, H., and Ajo-Franklin, J. B. On the Broadband Instrument Response of Fiber-Optic DAS Arrays. *Journal of Geophysical Research: Solid Earth*, 125(2), Feb. 2020. doi: 10.1029/2019jb018145.

Lontsi, A. M., Shynkarenko, A., Kremer, K., Hobiger, M., Bergamo, P., Fabbri, S. C., Anselmetti, F. S., and Fäh, D. A Robust Workflow for Acquiring and Preprocessing Ambient Vibration Data from Small Aperture Ocean Bottom Seismometer Arrays to Extract Scholte and Love Waves Phase-Velocity Dispersion Curves. *Pure and Applied Geophysics*, 179(1):105–123, Dec. 2021. doi: 10.1007/s00024-021-02923-8.

Lyberis, N., Angelier, J., Barrier, E., and Lallemant, S. Active deformation of a segment of arc: the strait of Kythira, Hellenic arc, Greece. *Journal of Structural Geology*, 4(3):299–311, Jan. 1982. doi: 10.1016/0191-8141(82)90016-5.

McClusky, S., Balassanian, S., Barka, A., Demir, C., Ergintav, S., Georgiev, I., Gurkan, O., Hamburger, M., Hurst, K., Kahle, H., Kastens, K., Kekelidze, G., King, R., Kotzev, V., Lenk, O., Mahmoud, S., Mishin, A., Nadariya, M., Ouzounis, A., Paradissis, D., Peter, Y., Prilepin, M., Reilinger, R., Sanli, I., Seeger, H., Tealeb, A., Toksöz, M. N., and Veis, G. Global Positioning System constraints on plate kinematics and dynamics in the eastern Mediterranean and Caucasus. *Journal of Geophysical Research: Solid Earth*, 105 (B3):5695–5719, Mar. 2000. doi: 10.1029/1999jb900351.

Melis, N. S., Lentas, K., and Schorlemmer, D. Seismic monitoring in Greece, 1899–2014: catalogue completeness 1966–2014. *Geophysical Journal International*, 235(2):1049–1063, July 2023. doi: 10.1093/gji/ggad285.

Miao, Y., Salaree, A., Spica, Z. J., Nishida, K., Yamada, T., and Shinohara, M. Assessing the Earthquake Recording Capability of an Ocean-Bottom Distributed Acoustic Sensing Array in the Sanriku Region, Japan. *Seismological Research Letters*, 96(2A):631–650, Sept. 2024. doi: 10.1785/0220240120.

Mykkeltveit, S. A new regional array in Norway: Design work and results from analysis of data from a provisional installation', The VELA program: A twenty-five yaer review of basic research. *Edited by U. A. Kerr (Defence Advanced Research Project Agency)*, pages 546–553, 1985.

Mykkeltveit, S. and Bungum, H. Processing of regional seismic events using data from small-aperture arrays. *Bulletin of the Seismological Society of America*, 74(6):2313–2333, 12 1984. doi: 10.1785/BSSA0740062313.

Métaxian, J., Lesage, P., and Dorel, J. Permanent tremor of Masaya Volcano, Nicaragua: Wave field analysis and source location. *Journal of Geophysical Research: Solid Earth*, 102(B10): 22529–22545, Oct. 1997. doi: 10.1029/97jb01141.

National Observatory of Athens, Institute of Geodynamics, Athens. Hellenic Unified Seismological Network, 1975. doi: 10.7914/SN/HL.

Näsholm, S. P., Iranpour, K., Wuestefeld, A., Dando, B. D. E., Baird, A. F., and Oye, V. Array Signal Processing on Distributed Acoustic Sensing Data: Directivity Effects in Slowness Space. *Journal of Geophysical Research: Solid Earth*, 127(2), Feb. 2022. doi: 10.1029/2021jb023587.

Ødegaard, E., Doornbos, D. J., and Kværna, T. Surface topographic effects at arrays and three-component stations. *Bulletin of the Seismological Society of America*, 80(6B):2214–2226, 12 1990. doi: 10.1785/BSSA08006B2214.

Okabe, A., Boots, B., and Sugihara, K. Spatial Tessellations: Concepts and Applications of Voronoi Diagrams. *The College Mathematics Journal*, 26(1):79, Jan. 1995. doi: 10.2307/2687299.

OpenTopography. Shuttle Radar Topography Mission (SRTM) Global, 2013. doi: 10.5069/G9445JDF.

Pichon, X. L. and Angelier, J. The hellenic arc and trench system: A key to the neotectonic evolution of the eastern mediterranean area. *Tectonophysics*, 60(1–2):1–42, Nov. 1979. doi: 10.1016/0040-1951(79)90131-8.

Pirli, M., Voulgaris, N., Chira, A., and Makropoulos, K. The March 2004 Kalamata seismic sequence: a case of efficient seismicity monitoring in the area of Peloponnese, southern Greece, by the Tripoli Seismic Array. *Journal of Seismology*, 11(1):59–72, Dec. 2006. doi: 10.1007/s10950-006-9037-8.

Pirli, M., Gibbons, S. J., and Schweitzer, J. Application of array-based waveform cross-correlation techniques to aftershock sequences: the 2003 Lefkada Island, Greece, case. *Journal of Seismology*, 15(3):533–544, Nov. 2010. doi: 10.1007/s10950-010-9216-5.

Pirli, M., Schweitzer, J., and Paulsen, B. The Storfjorden, Svalbard, 2008–2012 aftershock sequence: Seismotectonics in a polar environment. *Tectonophysics*, 601:192–205, Aug. 2013. doi: 10.1016/j.tecto.2013.05.010.

Ringdal, F. and Husebye, E. S. Application of arrays in the detection, location, and identification of seismic events. *Bulletin of the Seismological Society of America*, 72(6B):S201–S224, 12 1982. doi: 10.1785/BSSA07206B0201.

Rost, S. and Thomas, C. ARRAY SEISMOLOGY: METHODS AND APPLICATIONS. *Reviews of Geophysics*, 40(3), Sept. 2002. doi: 10.1029/2000rg000100.

Sambridge, M. Geophysical inversion with a neighbourhood algorithm—I. Searching a parameter space. *Geophysical Journal International*, 138(2):479–494, Aug. 1999. doi: 10.1046/j.1365-246x.1999.00876.x.

Sambridge, M. and Kennett, B. Seismic Event Location: Nonlinear Inversion Using a Neighbourhood Algorithm. *Pure and Applied Geophysics*, 158(1):241–257, Feb. 2001. doi: 10.1007/pl00001158.

Scholz, J.-R., Barruol, G., Fontaine, F. R., Sigloch, K., Crawford, W. C., and Deen, M. Orienting ocean-bottom seismometers fromP-wave and Rayleigh wave polarizations. *Geophys-*

ical Journal International, 208(3):1277–1289, Nov. 2016. doi: 10.1093/gji/ggw426.

Schweitzer, J. Tuning the automatic data processing for the Spitsbergen array (SPITS). 1998. doi: 10.21348/P.1998.0002.

Schweitzer, J. Slowness Corrections — One Way to Improve IDC Products. *Pure and Applied Geophysics*, 158(1):375–396, Feb. 2001. doi: 10.1007/pl00001165.

Schweitzer, J. and Kværna, T. Design Study for the Refurbishment of the SPITS Array (AS 72). 2002. doi: 10.21348/P.2002.0015.

Schweitzer, J., Fyen, J., Mykkeltveit, S., and Kværna, T. Seismic Arrays. 2009. doi: 10.2312/GFZ.NMSOP_r1_ch9.

Stachnik, J. C., Sheehan, A. F., Zietlow, D. W., Yang, Z., Collins, J., and Ferris, A. Determination of New Zealand Ocean Bottom Seismometer Orientation via Rayleigh-Wave Polarization. *Seismological Research Letters*, 83(4):704–713, July 2012. doi: 10.1785/0220110128.

Stump, B. Small-Aperture Seismo-Acoustic Arrays: Design, Implementation, and Utilization. *Bulletin of the Seismological Society of America*, 94(1):220–236, Feb. 2004. doi: 10.1785/0120020243.

Styron, R. and Pagani, M. The GEM Global Active Faults Database. *Earthquake Spectra*, 36(1S):160–180, Aug. 2020. doi: 10.1177/8755293020944182.

Trabattoni, A., Barruol, G., Dreo, R., Boudraa, A. O., and Fontaine, F. R. Orienting and locating ocean-bottom seismometers from ship noise analysis. *Geophysical Journal International*, Nov. 2019. doi: 10.1093/gji/ggz519.

Triantafyllis, N., Venetis, I. E., Fountoulakis, I., Pikoulis, E.-V., Sokos, E., and Evangelidis, C. P. Gisola: A High-Performance Computing Application for Real-Time Moment Tensor Inversion. *Seismological Research Letters*, 93(2A):957–966, Dec. 2021. doi: 10.1785/0220210153.

Vallée, M., Charléty, J., Ferreira, A. M. G., Delouis, B., and Vergoz, J. SCARDEC: a new technique for the rapid determination of seismic moment magnitude, focal mechanism and source time functions for large earthquakes using body-wave deconvolution: Wave deconvolution and earthquake parameters. *Geophysical Journal International*, 184(1):338–358, Nov. 2010. doi: 10.1111/j.1365-246x.2010.04836.x.

van den Ende, M. P. A. and Ampuero, J.-P. Evaluating seismic beamforming capabilities of distributed acoustic sensing arrays. *Solid Earth*, 12(4):915–934, Apr. 2021. doi: 10.5194/se-12-915-2021.

Veliz-Borel, V., Mouslopoulou, V., Nicol, A., Begg, J., and Oncken, O. Normal Faulting Along the Kythira-Antikythira Strait, Southwest Hellenic Forearc, Greece. *Frontiers in Earth Science*, 9, Jan. 2022. doi: 10.3389/feart.2021.730806.

Wei, X., Shen, Y., Caplan-Auerbach, J., and Morgan, J. K. An OBS Array to Investigate Offshore Seismicity during the 2018 Kīlauea Eruption. *Seismological Research Letters*, 92(1):603–612, Nov. 2020. doi: 10.1785/0220200206.

Wessel, P., Luis, J. F., Uieda, L., Scharroo, R., Wobbe, F., Smith, W. H. F., and Tian, D. The Generic Mapping Tools Version 6. *Geochemistry, Geophysics, Geosystems*, 20(11):5556–5564, Nov. 2019. doi: 10.1029/2019gc008515.

Zhu, G., Yang, H., Lin, J., and You, Q. Determining the Orientation of Ocean-Bottom Seismometers on the Seafloor and Correcting for Polarity Flipping via Polarization Analysis and Waveform Modeling. *Seismological Research Letters*, 91(2A):814–825, Feb. 2020. doi: 10.1785/0220190239.

Álvarez Gómez, J. A. FMC—Earthquake focal mechanisms data management, cluster and classification. *SoftwareX*, 9:299–307, Jan. 2019. doi: 10.1016/j.softx.2019.03.008.